

Extension of an orographic-drag parametrization scheme to incorporate orographic anisotropy and flow blocking

By YOUNG-JOON KIM* and JAMES D. DOYLE
Naval Research Laboratory, Monterey, California, USA

(Received 29 October 2004; revised 8 March 2005)

SUMMARY

The Kim–Arakawa orographic gravity-wave drag parametrization scheme, which is a component of the US Navy's NOGAPS ALPHA (Navy Operational Global Atmospheric Prediction System, Advanced-Level Physics and High Altitude), is extended to include the effects of orographic anisotropy and low-level flow blocking. The algorithms to calculate the orographic statistics needed for the parametrization are also revised. The extended scheme is evaluated against mountain waves explicitly simulated with COAMPS®† (Coupled Ocean/Atmosphere Mesoscale Prediction System) of NRL (Naval Research Laboratory).

Mountain-wave simulations over Boulder, Colorado, USA, are used for representing realistic situations of different wave activity including severe downslope windstorms. The simulations are area-averaged and interpolated to the vertical grid of NOGAPS, and are used as the input to the extended Kim–Arakawa scheme. The scheme is calibrated by comparing the parametrized vertical distribution of the momentum fluxes with the counterpart obtained from the explicit mesoscale simulations. Overall, the calibrated scheme successfully represents the simulated magnitudes and vertical divergences of the momentum fluxes. A flow regime diagram is constructed utilizing a time series of the simulations to further evaluate the parametrization. The robustness of the orographic statistics, together with an approximate method to improve it, are also addressed.

KEYWORDS: Blocked-layer drag Explicit gravity-wave simulation Form drag Gravity-wave drag Off-line evaluation Regime diagram Wave breaking

1. INTRODUCTION

The effects of orography can be represented by various means in large-scale models of the atmosphere, and their inclusion is crucial for successful simulation and forecast of weather and climate. Ever since the first generation gravity-wave drag (GWD) parametrization schemes based on the theories of two-dimensional (2-D), linear, hydrostatic, stationary mountain waves over an idealized isolated mountain were introduced, considerable progress has been made in improving the parametrizations. The most recent examples of such advancement are the inclusion of the effects of orographic anisotropy and low-level flow blocking.

Until recently, the effects of orography for the stably stratified atmosphere have been treated by separate parametrizations: the ‘breaking’ of unresolved gravity waves launched by subgrid-scale orography as presented by, e.g. Boer *et al.* (1984), Palmer *et al.* (1986) and McFarlane (1987), and the ‘blocking’ or ‘stagnation’ of low-level flow through enhanced resolved orography, which increases planetary wave forcing on the large-scale flow (e.g. Wallace *et al.* 1983; Iwasaki and Sumi 1986; Palmer and Mansfield 1986; Tibaldi 1986). The concept of ‘flow blocking’ was originally introduced into GWD parametrization in the mid 1980s. For a large (inverse) Froude number, $Fr_0 \ddagger$, associated with a relatively high mountain, the low-level flow is blocked by the mountain upstream, and the effective mountain height becomes lower than its actual value under

* Corresponding author: Naval Research Laboratory, Marine Meteorology Division, Stop 2, 7 Grace Hopper Avenue, Monterey, CA 93943, USA. e-mail: kimyj@nrlmry.navy.mil

† COAMPS is a registered trademark of the Naval Research Laboratory.

‡ The inverse Froude number is defined as $Fr_0 = hN_0/U_0$, where h is the mountain height, and N_0 and U_0 are the Brunt–Väisälä frequency and the horizontal wind magnitude, respectively, averaged over a depth which defines low levels. For GWD parametrization, h is usually defined as a multiple of the standard deviation of orography, σ_h , for a grid box.

© Royal Meteorological Society, 2005.

the 2-D framework (see Fig. 1, reproduced from Kim and Arakawa 1994). To account for this effect, Palmer *et al.* (1986) posed an upper limit on the height (400 m), while Pierrehumbert (1986) used an asymptotic flux function that gives a smooth transition between the blocking and non-blocking states; see Table 2 in Kim and Arakawa (1995, hereafter KA95) for a list of expressions to treat 2-D flow blocking. This concept of limiting the height of orography upstream was common among the first-generation parametrization schemes before the 3-D nature of orography was fully considered. In other words, the 2-D conceptualization of flow blocking considered only the flow 'over' the mountain, or the flow being blocked completely below the flow separation line that occurs on the mountain's flanks, whereas the more complete 3-D conceptualization also considers also the flow 'around' the mountain below the separation line (see Fig. 1 of Lott and Miller (1997), hereafter LM97).

Surface friction is known in general to reduce mountain-wave amplitudes and wave breaking aloft (e.g. Richard *et al.* 1989; Ólafsson and Bougeault 1997, hereafter OB97; Doyle *et al.* 2000; Leutbecher and Volkert 2000; Doyle and Durran 2002; Peng and Thompson 2003). Surface friction can be considered more important than GWD with regard to momentum exchange with the surface (e.g. Shutts and Broad 1993) and is often enhanced to represent the 'form drag' through increased effective surface roughness due to turbulence generated by subgrid-scale orography and vegetation under neutral conditions (e.g. Wood and Mason 1993; Milton and Wilson 1996, hereafter MW96; Belcher and Hunt 1998; Gregory *et al.* 1998, hereafter GSM98). This form drag concept has been extended to a scale larger than turbulence, where it was originally developed, to represent the drag generated by a layer of blocked flow under stable conditions due to flow past subgrid-scale orography (e.g. LM97; Scinocca and McFarlane 2000, hereafter SM00; Webster *et al.* 2003; Zadra *et al.* 2003; Alpert 2004; Brown and Webster 2004). As also pointed out by GSM98, the traditional definition of form drag refers to turbulence-scale orographic roughness under neutral or unstable conditions, whereas drag due to flow blocking is to account for subgrid-scale (larger than turbulence-scale) blocking or splitting of flow under stable conditions. In this study, therefore, we refer to the latter process as 'blocked-layer drag' (BLD). As a more physical alternative to the resolved-scale orographic height enhancement discussed above, a BLD parametrization is now implemented in a subgrid-scale sense, providing an additional source of low-level drag under the 3-D framework, and is often integrated as a part of GWD parametrization such as by LM97 and SM00.

The scheme proposed by KA95 parametrizes the drag due to breaking and trapping of both hydrostatic and non-hydrostatic gravity waves, and distinguishes between the 2-D flow-blocking 'upstream' state and wave breaking 'downstream' state based on Pierrehumbert's (1986) formulations, without incurring drag enhancement due to flow blocking in the 3-D sense. That is, the blocking due to stagnant flow formed upstream of orography reduces the effective height of orography, resulting in the decrease of drag, whereas low-level wave breaking (LLWB) or lee-wave trapping in the downstream region involves a significant increase in drag when certain flow conditions are met (Fig. 1). This scheme collectively treats any enhancement of GWD at low levels due to LLWB or lee-wave trapping in terms of the 2-D resonant amplification of GWD (Peltier and Clark 1979); it is physically similar to that of GSM98, but considers only partial effects of orographic anisotropy through additional orographic statistics. Its implementations into large-scale models are reported in Kim (1996; hereafter K96), Alpert *et al.* (1996) and also Kim and Hogan (2004).

The primary goal of the present study is to extend and evaluate the KA95 scheme by including 3-D effects of orography and also by including a BLD formulation.

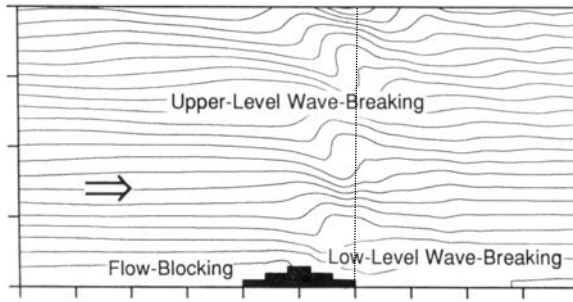


Figure 1. The key processes that the orographic gravity-wave drag (GWD) scheme of Kim and Arakawa (1995) attempts to parametrize. In the downstream region, low-level wave breaking and/or wave trapping of lee waves can contribute to GWD. The vertical dotted line is described in appendix A. (Taken from Kim and Arakawa (1994).)

We introduce a new orographic statistical parameter to consider the effect of orographic anisotropy. We derive the BLD formulation basically following earlier studies by LM97 and SM00, which are based on numerical studies of 3-D flow past isolated mountains (e.g. Hunt and Snyder 1980; Smolarkiewicz and Rotunno 1989; Miranda and James 1992, hereafter MJ92; Schär and Smith 1993; Ólafsson and Bougeault 1996, hereafter OB96; OB97; and Schär and Durran 1997). A rigorous evaluation of the parametrization with direct measurements is usually difficult due to limited availability and quality of high-resolution observation data. An alternative approach to evaluating the parametrization with observations is the use of a high-resolution mesoscale model, which has been evaluated by various means, e.g. against observational data and/or other verified model simulations as by, e.g. KA95, Broad (1996), LM97 and GSM98. In this study we evaluate the extended KA95 parametrization, hereafter KA95+, using explicit simulations of dry mountain waves obtained from a 3-D mesoscale model.

In section 2, we present the reformulated versions of orographic statistics originally developed for the KA95 scheme and also a new parameter for taking into account orographic anisotropy. In section 3, we summarize the KA95+ scheme; section 4 presents an evaluation of the scheme. We first describe our mesoscale model that explicitly simulates mountain waves, and present case-studies of the simulations representing typical mountain waves. We then evaluate the scheme using the cases by comparing simulated and parametrized results. We construct a regime diagram using all times of the simulations in an effort to further evaluate the scheme. We also discuss important issues regarding the robustness of the orographic statistics and the effects of moisture. Concluding remarks on remaining issues of the KA95+ scheme in particular and those of the GWD parametrization in general are given in section 5. Appendix A describes a non-local version of the parametrization scheme and appendix B introduces a method to obtain weighted averages of the orographic statistics.

2. STATISTICS OF SUBGRID-SCALE OROGRAPHY FOR THE KA95+ SCHEME

The KA95 scheme requires higher order statistics of orography as well as the standard deviation (σ_h) of subgrid-scale orographic heights. It utilizes the semi-empirical but geophysical relationships between the configuration of subgrid-scale orography and the physical characteristics of the corresponding flow, which were obtained from extensive 2-D mesoscale mountain-wave simulations involving over 100 cases with various shapes and sizes of mountains. Here, we discuss these orographic statistics.

(a) *Orographic asymmetry*

Lee waves that are trapped near the surface may propagate laterally to neighbouring grid cells, and similarly vertically propagating waves may traverse out of the original model column to neighbouring columns. Thus, GWD originating from a grid cell with orography may even influence a neighbouring cell with flat topography. As the resolution of models increases, this non-local nature of drag becomes more of a critical issue; however, current GWD parametrizations that assume a local column physics framework ignore this effect. This issue was addressed in Kim (1992) by introducing a new parameter which considers the effect of neighbouring grid domains (appendix A describes this issue further). This approach, however, introduces significant computational inefficiency under current parallel computing architecture due to the need for communication with neighbouring grid cells. Therefore, as a first step toward addressing the larger issue of non-local drag variance, KA95 incorporated this effect within a grid box, which is revisited here (for more discussion see appendix A).

The ‘orographic asymmetry’ (*OA*) measures the asymmetry of subgrid-scale orography and its relative location to the model grid box (see appendix B of KA95 for the original definition). We generalize the algorithm to calculate *OA* for any orographic data of any resolution, with either fixed intervals for grid point models or variable intervals for the Gaussian grid of spectral models:

$$OA \equiv 1 - (N^D/N^U), \quad (1)^*$$

where N^U and N^D denote, respectively, the numbers of subgrid-scale high-resolution orographic elevations in the upstream and downstream regions (relative to the wind direction) higher than the grid-box average of the orographic heights (which is a good approximation for high resolutions to the ‘mode’ used in K96, Eq. (B.1)). The calculations of N^U and N^D for the four representative wind directions (west, south, south-west and north-west) are illustrated in Fig. 2. Depending on the pre-determined directions of the low-level wind (zonal, meridional, or diagonal in either direction), the regions of the upstream and downstream areas are defined as shown in the figure. *OA* is obtained using Eq. (1) for the four representative directions, and *OA* (east, north, north-east and south-east) = $-OA$ (west, south, south-west and north-west), respectively (e.g. *OA* (east) is identical to $-OA$ (west)). In a large-scale model, *OA* is selected at each time step depending on the wind direction.

If the mountain is symmetric and located in the centre of the grid domain, *OA* is zero. Although the mountain is located in the centre of domain, however, *OA* becomes positive (negative) if the mountain is skewed to downstream (upstream) as illustrated in Figs. 3(a) and (b). This design is based on the 2-D mountain-wave simulations by KA95 and others showing that steeper slopes on the leeward sides involve stronger nonlinear waves and more likelihood for LLWB and/or non-hydrostatic wave trapping. *OA* can also distinguish between the two configurations of orography which involve the same mountain in the grid, but different locations relative to the grid (see Figs. 3(c) and (d))—one case including mostly downstream of the mountain ($OA > 0$) and the other upstream

* We limit the range of *OA* as in KA95 to prevent peculiarly large values due to a small number of orographic data points in a grid cell, so that $-1 \leq OA \leq 1$, which is typically found with real orographic data of any resolution. An alternative formula has been suggested (Dr N. Wood, personal communication), which does not require the arbitrary limit and ensures the anti-symmetry of *OA* for opposite wind directions even with a small number of orographic data points: $OA = c(N^U - N^D)/(N^U + N^D)$, where the case with $c = 3$ is then consistent with the original definition of Eq. (1).

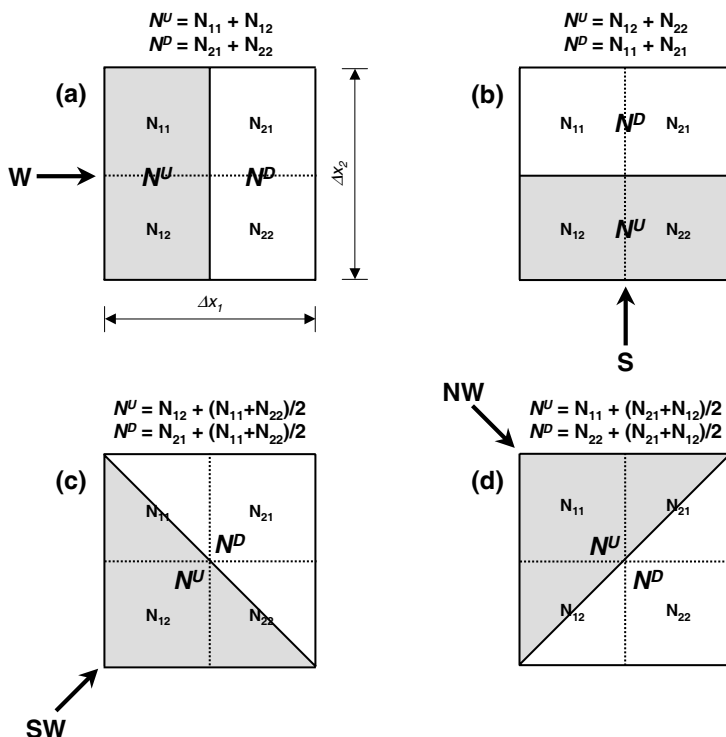


Figure 2. Method of dividing a grid box for calculating the numbers of the subgrid-scale orographic height data points in the upstream (N^U , shaded) and downstream (N^D) regions to be used for obtaining the orographic asymmetry (OA), depending on the low-level wind direction, i.e. (a) westerly, (b) southerly, (c) south-westerly, and (d) north-westerly. For the diagonal wind directions ((c) and (d)), two side subgrid boxes are summed and halved to be used both for the upstream and downstream regions. (Compare with Fig. 6.)

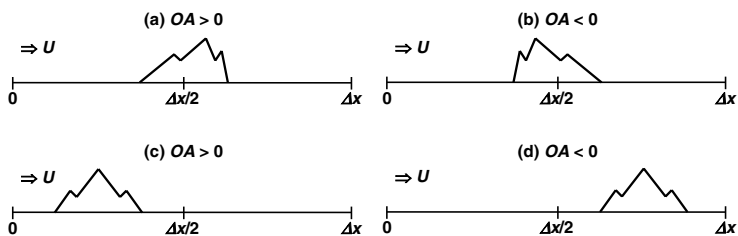


Figure 3. Illustration of orographic asymmetry (OA) for an isolated mountain sharing the same value of σ_h (standard deviation of topography) in the grid domain of side-length Δx . For a mountain that is symmetric and in the centre (not shown), OA is defined as zero. Although the mountain is centred, if it is skewed to (a) downstream ((b) upstream) OA is (a) positive ((b) negative). If the mountain is symmetric, but located toward the (c) upwind ((d) downwind) direction OA is (c) positive ((d) negative). Note that 2-D cases are shown here for simplified visualization, but the actual statistics are calculated for the grid-box area rather than for grid length Δx .

($OA < 0$). This is also based on results of the simulations by KA95 and others showing that downstream regions are more likely to contain stronger LLWB and/or non-hydrostatic wave trapping. The two idealized configurations shown in Figs. 3(c) and (d) share the same mountain in the same domain and thus are distinguishable not by the value of σ_h in the grid but by the values of OA with opposite sign. In the parametrization, a larger OA generally corresponds to a stronger GWD.

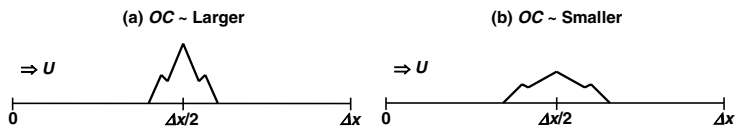


Figure 4. Illustration of orographic convexity (*OC*) for an idealized, symmetric and isolated mountain case in the grid domain of side-length Δx . A (a) sharper ((b) duller) mountain corresponds to (a) larger ((b) smaller) *OC*. Note that 2-D cases are shown here for simplified visualization, but the actual statistics are calculated for the grid-box area rather than for the grid length (Δx).

(b) *Orographic convexity*

The ‘orographic convexity’ (*OC*) represents the sharpness (and slope) of the mountain(s), which is linked to the characteristics of the corresponding mountain wave. The expression for *OC* taken from KA95 is:

$$OC \equiv (1/N_x \sigma_h^4) \sum_{i=1}^{N_x} (h_i - \bar{h})^4, \tag{2}$$

where x represents the horizontal direction, N_x denotes the number of subgrid-scale orographic height points within the large-scale grid, and the overbar denotes the large-scale grid average. The sharpness of mountain has been considered earlier in the parametrization by Phillips (1984). In general, a sharper (duller) mountain is associated with larger- (smaller-) amplitude waves (Fig. 4). As shown by KA95, *OC* is well correlated with the mountain’s ‘vertical aspect ratio’ (height to half-width; see Fig. 16 of KA95) in the case of isolated, symmetric mountains, which characterizes whether the waves are launched with characteristics of hydrostatic (low vertical aspect ratio) or non-hydrostatic (high vertical aspect ratio) waves.

(c) *Non-dimensional effective orographic length*

The ‘effective orographic length’ (L_x) is the subgrid-scale mountain width measured at the critical orographic height (h_c), which is integrated over the grid and normalized by the grid size (see Fig. 5). L_x was designed to complement Fr_0 , which alone cannot accurately measure the nonlinearity of the flow over complex mountains (KA95), by estimating the bulk volume of subgrid-scale orography that is associated with non-linearity of the flow. Strongly nonlinear flow with larger Fr_0 involves smaller h_c , and thus larger L_x . K96 used the expression, $h_c = 1116.2 - 0.878\sigma_h$, which was empirically derived from the 2-D mountain-wave simulations of KA95, to avoid calculating h_c in every time step using the original definition, $\sigma_h Fr_c / Fr_0$, where $Fr_c (\approx 0.8)$ is a prescribed critical Froude number. In this study we further assume, based on some earlier tests, that the grid-box average of the subgrid-scale orographic heights is a crude approximation to the empirical value of h_c and now use the average in calculating L_x .

The expression for L_x described by KA95 is generalized here as:

$$L_x \equiv \sum_i L_{xi} / \Delta x = N^W / N^T. \tag{3}$$

Here, Δx is the horizontal grid size, N^W denotes the number of subgrid-scale orographic heights (high-resolution elevation data points) along the centre area with respect to the wind crossing over four one-eighth grid boxes (for the directions west and south; Figs. 6(a) and (b)) or two one-quarter grid boxes (for south-west and north-west;

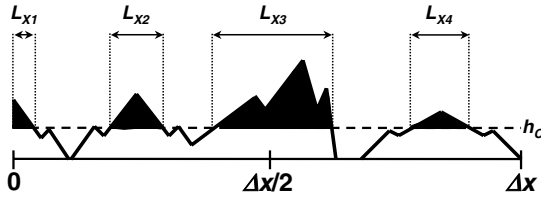


Figure 5. Illustration of the non-dimensional effective orographic length ($L_x = \sum_i L_{xi} / \Delta x$), which is the sum of the non-dimensionalized horizontal lengths intersecting the subgrid-scale mountain at the critical height (h_c) in the grid of length Δx . h_c is approximated in this study by the grid-box (area) averaged value of subgrid-scale orographic heights. The value of L_x is calculated for the four representative low-level wind directions (described in Fig. 6). Note that here 2-D cases are shown for simplified visualization, but the actual statistics are calculated for the grid-box area rather than for (Δx) .

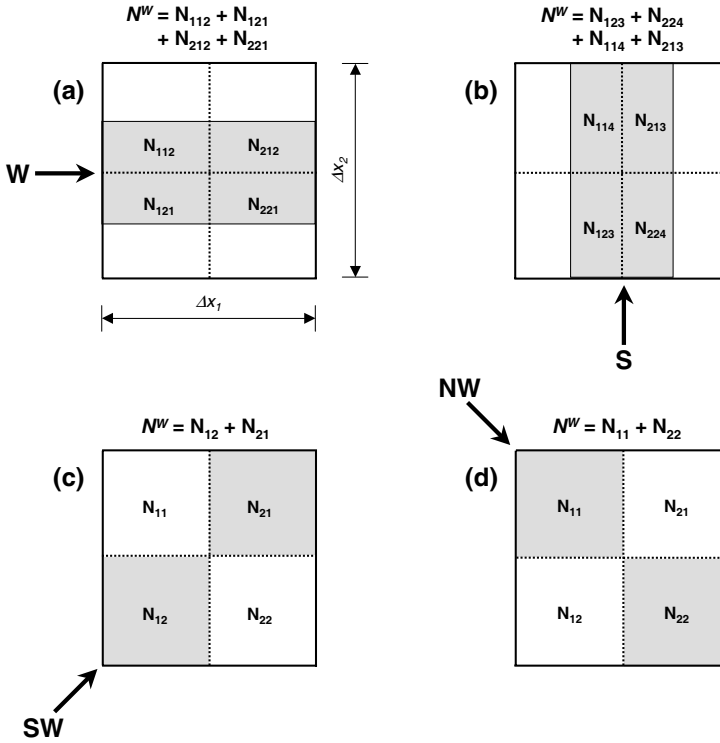


Figure 6. Methods of dividing a grid box for calculating the number of subgrid-scale orographic height data points in the grid box higher than the grid average (N^W) to be used for obtaining the effective orographic length, L_x . The total number of orographic height data points (N^T), which is also needed to obtain L_x (see Eq. (3)), is counted for the same subgrid-scale boxes as for N^W . Depending on the low-level wind direction, four one-eighth boxes or two one-quarter boxes (shaded) are regarded as the centre section of the box in the direction of the flow.

Figs. 6(c) and (d)), which are higher than the grid average (both considering effectively the half of the grid box area as shaded in the figure). N^T denotes the total number of orographic data points in the grid box. The calculation is performed for the four representative wind directions similarly to that of OA , and L_x (east, north, north-east and south-east) = L_x (west, south, south-west and north-west), respectively. In a large-scale model, L_x is selected at each time step depending on the wind direction.

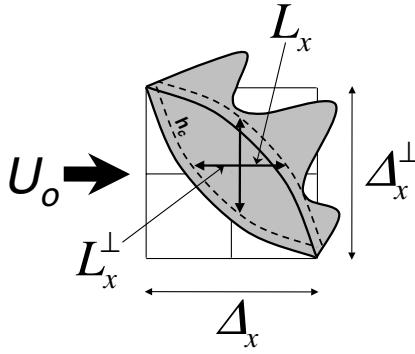


Figure 7. Illustration of the length of the large-scale grid (Δ_x) and the subgrid-scale effective orographic length (L_x) in the direction of the low-level wind (U_0) for an isolated mountain; also the lengths in the direction perpendicular to the low-level wind (Δ_x^\perp and L_x^\perp , respectively). The critical orographic height, h_c , which is approximated by the grid mean orographic height in this study, is shown by the dashed line. The orographic direction (OD), defined by Eq. (4), is calculated using L_x and L_x^\perp .

(d) Orographic direction

It is known that 3-D spreading of mountain waves tends to reduce wave momentum fluxes and GWD above (e.g. Shutts 1998). It was reported that idealized 3-D orography generates only about the half of the momentum flux in comparison with corresponding 2-D orography (Nappo and Chimonas 1992). Orographic anisotropy was earlier included in the GWD parametrizations by Baines and Palmer (1990) and Shutts (1990). The KA95 scheme was originally calibrated based on a 2-D framework using simulations with a 2-D mountain-wave model. The 3-D effects of orography were considered only partially through OA and L_x , which were calculated for the eight representative wind directions as described above. Thus the KA95 scheme did not fully consider the reduction of wave amplitude due to orographic anisotropy. As a result, the low-level Froude number ($Fr_0 = hN_0/U_0$), which is one of the major measures of nonlinearity of the flow for the parametrization, inherently assumed the mountain of infinite length in the cross-wind direction. To rectify this deficiency, we introduce ‘orographic direction’ (OD) representing the orographic anisotropy:

$$OD \equiv \frac{L_x^\perp}{L_x}, \quad (4)$$

where superscript \perp denotes the cross-wind direction, i.e. L_x^\perp denotes L_x for the direction perpendicular to the low-level wind (see Fig. 7). OD is equivalent to the mountain’s ‘horizontal aspect ratio’ (cross-width to along-width) or inverse ‘eccentricity’ (SM00) for a single symmetric mountain, but is defined more generally here as dominant bulk subgrid-scale orography summed over the grid box with respect to the representative wind directions. The Froude number is accordingly redefined as:

$$Fr_0 \equiv h \frac{N_0}{U_0} OD, \quad (5)$$

where the orographic height, h , is defined as $2\sigma_h$ in this study.

(e) Orographic statistics database

The orographic statistics systematically consider the details of subgrid-scale orography (e.g. shape, size, number, distribution, direction, etc). These statistics are

designed to be calculated offline for computational efficiency. First, OC and σ_h , which do not depend on the wind direction, are calculated. Then, lookup tables of OA , OD and L_x with respect to the representative four low-level wind directions (west, south, south-west and north-west) are constructed. For consistency, these orographic statistics derived from the revised algorithms have been compared for the 2-D ridge cases with those from the original algorithms of KA95. When used online in a large-scale model, the parametrization scheme first determines the direction of the low-level wind at each time step, and then simply looks up the pre-calculated tables to find the corresponding orographic statistics.

3. EXTENSION OF THE KA95 OROGRAPHIC GWD PARAMETRIZATION SCHEME

(a) *The gravity-wave drag parametrization*

The formulations for the GWD parametrization are formally the same as those of KA95 and K96 except that Fr_0 is now multiplied by OD to include the effects of orographic anisotropy as shown in Eq. (5). The GWD (τ) at the reference level (h_{ref}) is:

$$\tau_{\text{GWD}} = \rho_0 E \frac{m}{\lambda_{\text{eff}}} G \frac{|U_0|^3}{N_0}, \quad (6)$$

$$E \equiv (OA + 2)^{C_E Fr_0 / Fr_c}, \quad m \equiv (1 + L_x)^{OA+1}, \quad G \equiv \frac{Fr_0^2}{Fr_0^2 + C_G OC^{-1}}, \quad (7)$$

where ρ is the density; N is the Brunt–Väisälä frequency, U is the horizontal wind speed projected to the direction of the low-level wind; E is the ‘enhancement factor’ applied only at the reference level to represent the nonlinear enhancement of drag by resonant amplification (e.g. Peltier and Clark 1979) in the downstream regions due to LLWB and/or wave trapping, and is controlled by the shape and location of subgrid-scale orography in the grid (OA) and the nonlinearity of the grid-scale flow (Fr_0) normalized by its critical value; m is the ‘number of mountains’, which estimates the bulk volume of subgrid-scale orography associated with the nonlinearity of the flow (L_x), and depends also on the shape and location of subgrid-scale mountain(s) relative to the grid (OA); G is an asymptotic function that provides a smooth transition between 2-D non-blocking and blocking cases as used by Pierrehumbert (1986) and includes the influence of the vertical mountain aspect ratio through OC , empirically applying the original idea by Pierrehumbert (1986; Eq. (3.8)); and λ_{eff} is the effective grid length, which was set to the length of the grid box in K96, but can be used practically as a tuning coefficient. We set $C_E = 0.8$ and $C_G = 0.5$ as originally calibrated with mesoscale simulations (KA95). The subscript o denotes a low-level average, which in this study is between the surface and $2\sigma_h$ ($=h$) differing from the original definition in K96 of the depth of the atmospheric boundary layer. The expressions in Eq. (7) were derived semi-empirically based on physical concepts and evaluated against extensive 2-D mountain-wave simulations (KA95).

A nonlinear extension of the original Pierrehumbert formulation, $m \cdot E$, becomes larger as OA increases, in order to be consistent with the simulations of KA95 that indicate downstream regions are more likely to include stronger wave activity, and thus a greater chance for drag enhancement. KA95 demonstrated that $m \cdot E$ accurately represents at low levels (see Figs. 18(c) and 25 of KA95) the vertical gradient of the Scorer parameter (Scorer 1949), which can be approximated as $\ell^2 \approx N^2/U^2$ (more rigorous definitions are given by, e.g. KA95 footnote 7, or Nance and Durran (1998)

Eq. (4)). Analytical and numerical simulation studies of mountain waves show that the Scorer parameter influences the linear resonant trapping of non-hydrostatic waves (lee waves) at low levels (e.g. Bretherton 1969; Shutts and Broad 1993; Doyle *et al.* 2002). KA95 further found that it also serves as a good measure of nonlinear resonant LLWB. Whether of linear or nonlinear nature, this wave activity at low levels contributes to increased vertical divergence of GWD. KA95 demonstrated that the vertical gradient of the Scorer parameter cannot be uniquely parametrized by Fr_0 —the main flow parameter used in earlier conventional GWD schemes—for different situations, say, with or without LLWB (see Fig. 13 of KA95). Peng and Thompson (2003) also questioned whether Fr_0 in GWD parametrizations could properly represent boundary-layer processes.

A model layer is considered unstable if the minimum Richardson number defined by:

$$Ri_m = \frac{Ri(1 - Fr_d)}{(1 + \sqrt{Ri} Fr_d)^2} \quad (8)$$

becomes less than its critical number, i.e. if $Ri_m < Ri_c$ (typically, $Ri_c \simeq 0.25$), where Ri is the (mean) Richardson number, (defined by Eq. (2.11) in KA95) and $Fr_d \equiv h_d N / U$. Here, the vertical displacement height, h_d , is expressed combining the expressions by Palmer *et al.* (1986) and Pierrehumbert (1986) as:

$$(h_d^2)_i = \frac{\Delta x}{m} \frac{\tau_{i+1}}{\rho_i N_i U_i}, \quad (9)$$

where subscript i denotes the vertical-layer index decreasing upward. The expression for the critical value of h_d is then derived by substituting $Ri_c = 0.25$ into Eq. (8) as:

$$(h_d)_c = \frac{U}{N} \left\{ 2 \left(2 + \frac{1}{\sqrt{Ri}} \right)^{1/2} - \left(2 + \frac{1}{\sqrt{Ri}} \right) \right\}. \quad (10)$$

The profile of GWD is determined according to the following steps (see KA95 for more details):

- The reference-level drag, τ_{GWD} , is calculated from Eq. (6).
- The vertical displacement height, h_d , is computed by Eq. (9).
- The layer stability is checked by evaluating Ri_m using the computed h_d in Eq. (8).
- If $Ri_m > Ri_c$, τ is unchanged for the next model layer, whereas, if $Ri_m \leq Ri_c$, τ is calculated from Eq. (9) (with $i + 1$ replaced by i) using $(h_d)_c$ obtained from Eq. (10).

It was shown by KA95, based on 2-D mountain-wave simulations, that LLWB or wave trapping is not properly represented by the saturation hypothesis of Lindzen (1981), but is better represented by the vertical gradient of the Scorer parameter. For this reason, KA95 determined the vertical decrease of the drag at low levels (below the ‘interface height’, h_{int}) by the ratio of the Scorer parameter instead of the saturation hypothesis when the Ri criterion is met in a model layer as:

$$\frac{\tau_i}{\tau_{i+1}} = \text{Min} \left(C_\ell \frac{\ell_i^2}{\ell_{i+1}^2}, 1 \right), \quad (11)$$

where $C_\ell = 1$, and h_{int} is now defined as the level where Ri first decreases with height above the reference level. Moreover, this ratio is now applied regardless of OA , unlike K96 who used the ratio only for $OA > 0$, in order to ensure a smoother transition between the upstream and downstream configurations.

(b) *The blocked-layer drag parametrization*

In the introduction, we discussed the recent advances in the GWD parametrization community that includes an extra source of drag due to flow blocking at low levels in place of enhanced resolved orography. Along these lines, we extend KA95 by including BLD in the drag parametrization. Our formulation basically follows previous pioneering parametrization studies (e.g. LM97, SM00) and takes the following bulk aerodynamic drag form, which is based in part on scale analysis and is particularly similar to that of SM00; however, some key parameters are calculated using distinctly different methods:

$$\tau_{\text{BLD}} = \frac{1}{2} \rho_0 \frac{m}{\Delta_x^2} C_d \Delta_x^\perp L_x^\perp h_B |U_0|^2, \quad (12)$$

where Δ_x^2 is the grid box area, C_d is a bulk drag coefficient of order unity (we set $C_d = 1$ in this study), Δ_x^\perp is the length of large-scale grid in the cross-wind direction, and L_x^\perp is as used in Eq. (4) the width of dominant subgrid-scale orography along the cross-wind direction, which is approximated as the width of orography measured at the critical orographic height (see Fig. 7); h_B is the height of blocked layer defined as:

$$h_B \equiv \frac{U_0}{N_0} (Fr_0 - Fr_c) > 0. \quad (13)$$

The orographic anisotropy is considered through h_B that includes Fr_0 (Eq. (13)), which itself is multiplied by OD (Eq. (5)). The BLD is calculated using Eq. (12) when $Fr_0 > Fr_c$, and applied to the lowest model level above the surface and linearly decreased in height as in other studies. (More details are given in subsection 4(c).)

4. EVALUATION OF THE KA95+ SCHEME WITH EXPLICIT MOUNTAIN-WAVE SIMULATIONS

(a) *Mesoscale model COAMPS[®]*

For explicit simulations of mountain waves, we use the atmospheric component of COAMPS[®] (Hodur 1997). This mesoscale model uses finite-difference approximations to describe the fully compressible, non-hydrostatic equations that govern atmospheric motions, and a terrain-following vertical coordinate. The prognostic variables of the model are the horizontal velocity, vertical velocity, perturbation Exner function, potential temperature, turbulent kinetic energy, and the concentrations of moisture, cloud drops, ice crystals, snow, rain, graupel and aerosols. The horizontal and vertical advection, pressure gradient, and divergence are represented by second order accurate differencing in this application. Nonlinear instability is suppressed by a fourth-derivative hyper-diffusion. Turbulent processes are represented by a level-2.5 closure parametrization, similar to the level-1.5 turbulence closure scheme used in KA95's dry mountain-wave model, which was essential for proper development of mountain waves with large amplitudes. Lateral boundary conditions make use of the Navy Operational Global Atmospheric Prediction System (NOGAPS, Hogan and Rosmond 1991) forecast fields following Davies (1976). The nested-grid boundary conditions are formulated using a one-way-interaction approach with a horizontal resolution of each nested mesh that is 1/3 of the parent grid mesh.

Shutts and Broad (1993) and Broad (1996) performed simulations using a mesoscale model with simplified physics, and compared the results to those from a GWD parametrization based on dry mountain-wave theory. In these simulations, the relative

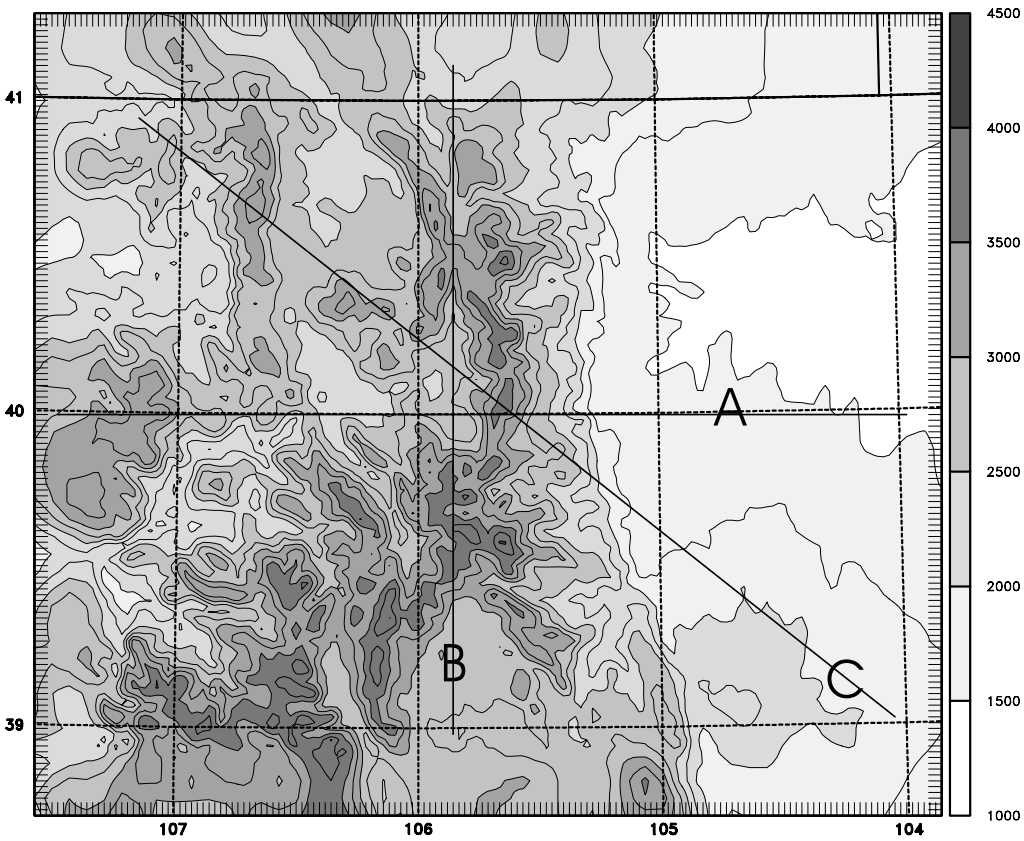


Figure 8. The terrain field (m) for the domain near Boulder, Colorado, USA, used for simulating mountain waves with COAMPS® (Coupled Ocean/Atmosphere Mesoscale Prediction System of the Naval Research Laboratory). The three solid lines denote the lower boundaries of the vertical cross-sections for Cases A (06 UTC 28 December 1998), B (00 UTC 31 October 1998) and C (12 UTC 01 January 1999). Abcissa and ordinate are degrees of longitude and latitude, respectively.

humidity was set to 1% to avoid cloud formation and precipitation, the surface heat-exchange coefficient was set to zero to suppress surface energy transfer, and radiative forcing was not allowed in order to perform a meaningful comparison. Similarly, in this study we limit these processes in COAMPS® in order to obtain the dry mountain-wave response, except for a test case to see the impact of moisture as is discussed in subsection 4(f).

(b) Dry mountain-wave simulations

We simulated three mountain-wave events over Boulder, Colorado, USA (see topographical details in Fig. 8). This region is famous for frequent occurrence of strong downslope windstorms along the lee side of the Rockies (e.g. Lilly and Zipser 1972). We consider the innermost nested-grid domain of the model, which spans latitudes 38.70–41.26°N and longitudes 107.63–103.78°W. The vertical domain reaches 24 570 m in height. The horizontal resolution is 2000 m with 157×139 grid points, and the vertical resolution varies between 10 m at the surface and 500 m at the top with 60 levels.

We integrated the model starting from three different dates: 00 UTC 28 December 1998, 00 UTC 30 October 1998 and 00 UTC 01 January 1999, using the lateral boundary

TABLE 1. DETAILS OF THE THREE CASE-STUDIES OF MOUNTAIN WAVE SIMULATIONS WITH COAMPS®

	Case A	Case B	Case C
Initialization time	00 UTC 28 December 1998	00 UTC 30 October 1998	00 UTC 1 January 1999
Snapshot time	06 UTC 28 December 1998	00 UTC 31 October 1998	12 UTC 1 January 1999
Low-level wind angle from north (°)	282	165	308
Low-level wind direction	Westerly	Southerly	North-westerly
Δ_x (km)	428.5	284.3	514.2
Δ_x^\perp (km)	284.3	428.5	514.2
σ_h (m)	625.1	625.1	625.1
OA	0.73	0.27	0.34
OC	2.02	2.02	2.02
OD	1.43	0.70	1.01
L_x	0.48	0.69	0.52
L_x^\perp	0.69	0.48	0.52
Fr_0	1.30	1.02	1.32
N_0 (s ⁻¹)	1.27×10^{-2}	1.44×10^{-2}	1.00×10^{-2}
U_0 (m s ⁻¹)	17.45	10.36	9.56
m	1.98	1.95	1.75
E	3.70	2.71	3.08
λ_{eff} (km)	3000	3000	3000
$\kappa (= m/\lambda_{\text{eff}})$ (m ⁻¹)	6.58×10^{-7}	5.00×10^{-6}	5.83×10^{-7}
h_{int} (m)	6357.6	5609.4	5162.9
h_{ref} (m)	4783.7	4835.6	4794.5
h_B (m)	3063.5	2673.5	2870.9

See text for the definitions of parameters. The height values are measured from mean sea level, while the surface level is at 2373.2 m.

conditions provided by NOGAPS forecasts. When the mountain waves were fully developed, we examined three episodes: Case A at 06 UTC 28 December 1998, Case B at 00 UTC 31 October 1998, and Case C at 12 UTC 01 January 1999, where the low-level average wind is approximately perpendicular, parallel, and at a significant angle to the approximate ridge axis of the mountain range, respectively. The mountain range is oriented approximately north–south in the centre of the domain (see Table 1 for details of the simulations).

(i) *Case A simulation (06 UTC 28 December 1998)*. The terrain and typical atmospheric conditions of the Boulder area (Fig. 8) are generally favourable for strong wave generation. At 06 UTC 28 December 1998, the low-level wind direction is westerly at the mountain crest level, nearly perpendicular to the approximate centre line of the ridge. The winds are stronger over the highest peak of the mountain range, as shown in the vertical cross-section of the wind and isentropes (Fig. 9(a)) corresponding to line A in Fig. 8. This is associated with strong wave-breaking, which first occurs around 7 km over the steep lee-side slope of the highest peak and subsequently propagates down to the surface, as is clearly shown by steepened isentropes and increased zonal winds (Fig. 9(a)). This downslope windstorm is accompanied by weak or reversed flow in the region of wave breaking itself (shown by light colours) above the accelerated flow region.

(ii) *Case B simulation (00 UTC 31 October 1998)*. At 00 UTC 31 October 1998, the direction of the low-level wind is largely from the south approximately parallel to the mountain ridge. As a result, the low-level flow does not encounter major orography in the eastern half of the domain. The wave activity near the surface is weaker in Case B (Fig. 9(b)) than in Case A (Fig. 9(a)) since the low-level flow is weaker due to the orographic configuration in the upstream region (see the southern centre region along

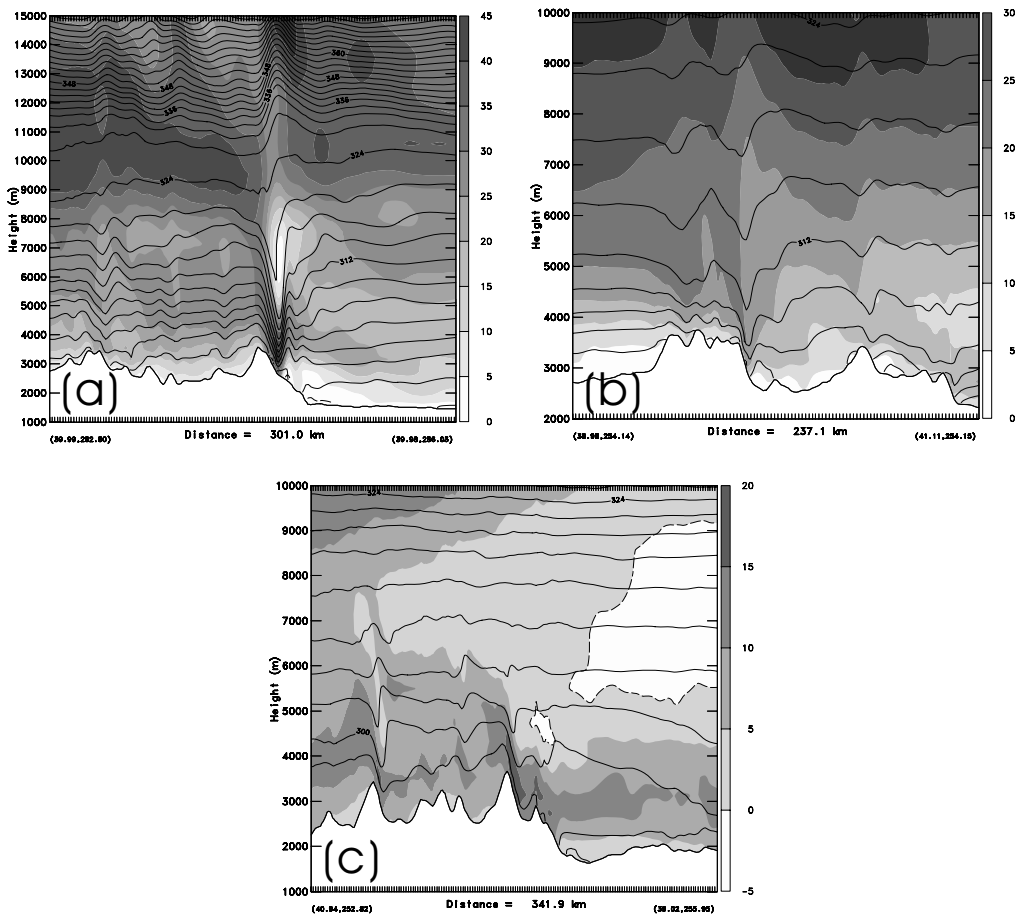


Figure 9. Vertical cross-sections showing contours of potential-temperature (K) and zonal wind (m s^{-1} , grey shades—see key) simulated by COAMPS[®] (Coupled Ocean/Atmosphere Mesoscale Prediction System of the Naval Research Laboratory) along the lines shown in Fig. 8: (a) Case A (06 UTC 28 December 1998); (b) Case B (00 UTC 31 October 1998); and (c) Case C (12 UTC 01 January 1999). The low-level flow is from left to right, which is from: (a) west to east, (b) south to north, and (c) north-west to south-east. The zero zonal wind contours are denoted by long dashed lines. Note that the vertical scale of (a) is different from those of (b) and (c).

line B in Fig. 8) that largely blocks the low-level flow (clearly seen from the cross-section of the wind at 3000 m; not shown). There is, however, still significant wave activity especially downstream of the major mountain peak (Fig. 9(b)).

(iii) *Case C simulation (12 UTC 01 January 1999)*. At 12 UTC 01 January 1999, the low-level winds are primarily north-westerly; thus this case lies between Cases A and B with respect to the low-level wind direction. In view of the orographic variations, the vertical cross-section for line C (Fig. 8) passes through several relatively narrow peaks (Fig. 9(c)) and has a relatively deep downslope region in the downstream half of the cross-section, which causes a fairly strong downslope windstorm over the lee side of the highest peak in the centre. The zonal winds over the downslope of the highest peak are stronger than in the surrounding area as a result of LLWB, although weaker than Case A. Unlike the other cases the waves do not propagate much vertically as can be seen from the relatively flat isentropes in the upper part of Fig. 9(c). There are two distinct

regions of zonal flow reversal: one is in the lee of the highest peak; the other is over the downstream end of the cross-section between about 5.5 km and 9 km, shown in Fig. 9(c) inside long dashed contours. The first region seems to be a direct result of wave activity at low levels, whereas the second is due to the turning of the wind direction from north-westerly to south-westerly with height associated with a front along the downstream half of the cross-section (not shown).

(c) *Offline evaluation of the KA95+ scheme using the explicit simulations*

We now evaluate the KA95+ orographic GWD parametrization scheme using explicit COAMPS® simulations basically following KA95. The evaluation procedure consists of the following key steps:

- The horizontal angles of simulated low-level winds are domain-averaged over the depth of $2\sigma_h$.
- The zonal, meridional and vertical components of the simulated winds are decomposed into their area means (overbar) and deviations (prime) from the means.
- The horizontal momentum fluxes are calculated at each point, projected to the averaged low-level wind direction, area-averaged, and vertically interpolated to large-scale model pressure levels ($\overline{\rho u'w'}^S$).
- The KA95+ scheme is applied to the area-averaged and vertically interpolated simulated variables, also using the orographic statistics calculated from the topography used in the simulations, to parametrize the momentum flux profile ($\overline{\rho u'w'}^P$).
- The parametrized momentum flux profile ($\overline{\rho u'w'}^P$) is compared with the explicitly simulated momentum flux profile ($\overline{\rho u'w'}^S$).
- In addition, below the reference level, the total parametrized surface drag (GWD plus BLD, as discussed by Webster *et al.* (2003)) is compared with the explicitly simulated surface pressure drag, both of which are linearly interpolated in the vertical and connected to the flux profile at the reference level (similar to Lane *et al.* 2000).

(i) *Evaluation of Case A (06 UTC 28 December 1998).* We first evaluate Case A in which the low-level wind is oriented perpendicular to the mountain ridge axis, which is thus a good test case for a quasi 2-D situation with strong LLWB ($Fr_0 = 1.30 > Fr_c$; see Table 1, Fig. 9(a)). The low-level wind, which is the average between the surface and the height of $2\sigma_h$ (between 2373 and 3623 m above sea level, or 1250 m from the surface) is westerly, which is used by the parametrization at the reference level. Figure 10 shows the domain-averaged profiles of the buoyancy frequency and projected wind, which are key input parameters to the scheme (note that this average is not just for the cross-section, but for the entire domain, following Broad (1996)). An approximate two-layered structure is evident, which is typically found in the atmosphere with strong resonant waves. The atmospheric static stability for Case A (Fig. 10(a)) first increases and then decreases with height in the lower part of the domain, then rapidly decreases from around 11 km, and gradually increases further up. The projected wind for Case A (Fig. 10(b)) forms a positive shear up to about 11 km and a negative shear above that. Figure 11 shows the minimum Richardson number (Eq. (8)), which describes the instability of the layers as diagnosed by the parametrization. This graphically shows that the layer instability (Ri_m) depends sensitively on its critical value (we use $Ri_c = 1$ as in LM97; $Ri_c = 0.25$ was used by KA95 and K96).

Figure 12(a) first compares the simulated and parametrized momentum flux profiles. (The ‘weighted’ parametrization is discussed later in subsection 4(e).) Note that

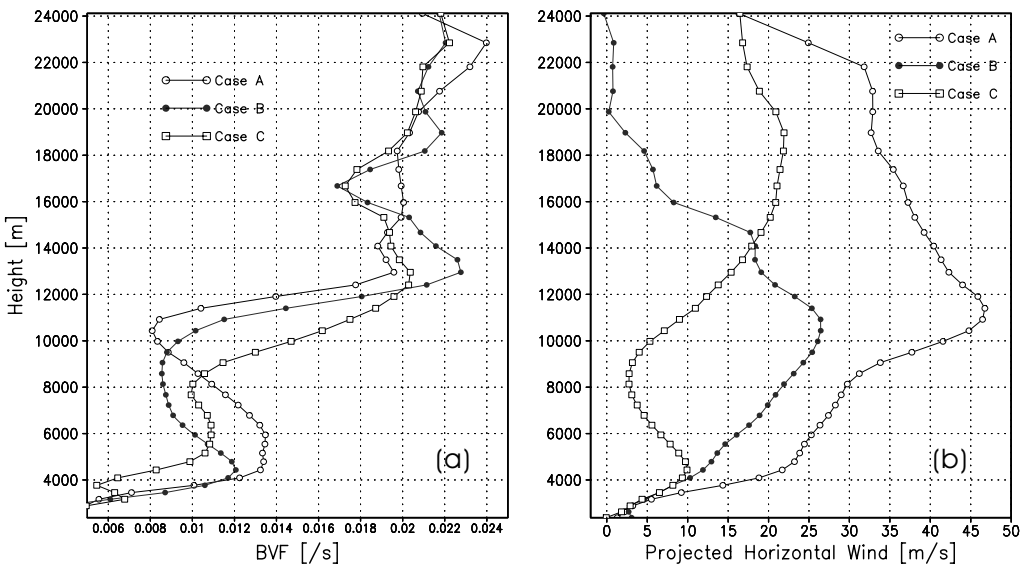


Figure 10. Profiles for Cases A (06 UTC 28 December 1998), B (00 UTC 31 October 1998) and C (12 UTC 01 January 1999) of the domain-averaged: (a) Brunt–Väisälä frequency, and (b) horizontal wind projected on to the direction of the low-level wind average. Simulations profiled are by COAMPS® (Coupled Ocean/Atmosphere Mesoscale Prediction System of the Naval Research Laboratory).

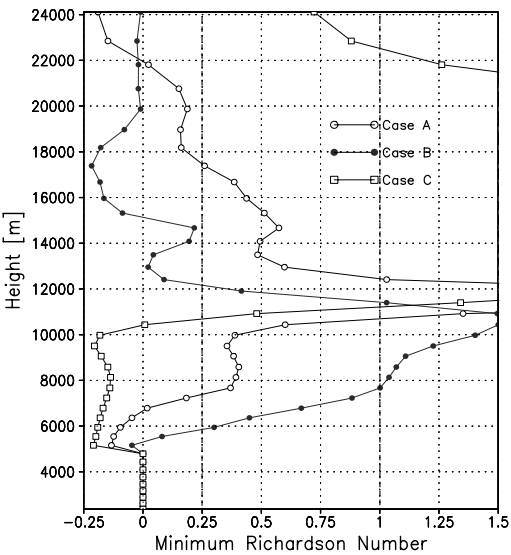


Figure 11. Profiles of the minimum Richardson number for Cases A (06 UTC 28 December 1998), B (00 UTC 31 October 1998) and C (12 UTC 01 January 1999). See text for details.

the parametrized BLD at the surface (plus GWD, which is assumed constant with height below the reference level) has been linearly interpolated to the parametrized flux profile due to GWD at the reference level (denoted by the horizontal line), while the surface pressure drag, calculated in the direction of the low-level wind, has been linearly interpolated to the simulated flux profile. Although there exist some differences in the

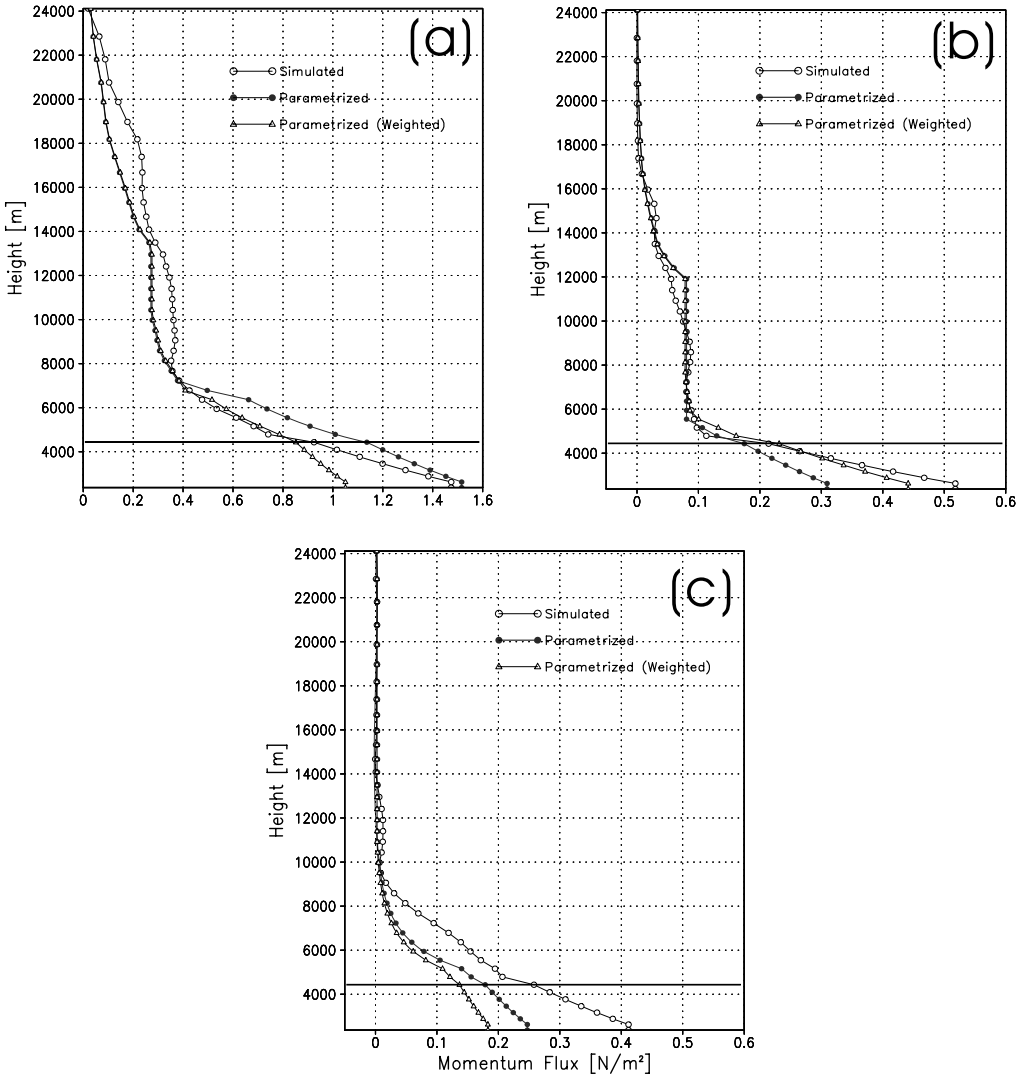


Figure 12. Profiles of the simulated (open circles), parametrized (closed circles) and parametrized with weighted orographic statistics (triangles) vertical fluxes of the horizontal momentum for: (a) Case A (06 UTC 28 December 1998), (b) Case B (00 UTC 31 October 1998) and (c) Case C (12 UTC 01 January 1999). The sign of the momentum fluxes is reversed following the convention of the parametrization scheme. The profiles below the horizontal line are linear fits of the surface pressure drag (simulated) and the blocked-layer drag plus gravity-wave drag (parametrized) to the reference-level drag. Note that the horizontal scale of (a) is different from those of (b) and (c). See text for further details.

details, the matching between the two profiles is excellent for this case. The use of $Ri_c = 1$ is found helpful for this case in detecting wave-breaking at upper levels where Ri_m is mostly larger than 0.25 (see Fig. 11). The results with $Ri_c = 0.25$ or 0.5 are still in reasonable agreement overall (not shown), but inferior to the result with $Ri_c = 1$ at upper levels.

(ii) *Evaluation of Case B (00 UTC 31 October 1998).* We next evaluate Case B in which the low-level wind direction is southerly and nearly parallel to the average

ridge axis (Fig. 9(b)). This case is thus selected to represent an extreme 3-D anisotropic situation. The flow is fairly nonlinear ($Fr_0 = 1.02 > Fr_c$, see Table 1) due to the characteristics of the Front Range of the Rockies. The variation of orography is significant both in the along-flow (south–north) and cross-flow (west–east) directions (Fig. 8). The horizontal domain averages of the static stability and projected horizontal wind are similar to Case A, and show a two-layered structure with weaker winds above 11 km (Fig. 10).

The simulated and parametrized momentum flux profiles compare well (for $Ri_c = 1$) except below the reference level (Fig. 12(b)), and are not greatly sensitive to the choice of Ri_c since Ri is mostly smaller than 0.25 when the layer is unstable (Fig. 11). It is noted that the magnitude of the flux for Case B at the reference level is about an order of magnitude smaller than that for Case A; this is a result of weaker LLWB due to the 3-D anisotropic configuration of orography. The value of OD (0.7 for Case B versus 1.43 for Case A, see Table 1) successfully controls the magnitude of parametrized GWD, which would have been overestimated if OD were not used. There is, however, a significant difference between the two profiles below the reference level due to the BLD parametrization, although they are within the same order of magnitude (Fig. 12(b)). The parametrized BLD is about half of the calculated surface pressure drag.

(iii) *Evaluation of Case C (12 UTC 01 January 1999)*. We now evaluate Case C in which the low-level wind is oriented half-way between Cases A and B. This is a good test case for a situation in which the flow is at an angle with respect to the mountain ridge axis. The averaged low-level wind is north-westerly and the flow is also strongly nonlinear ($Fr_0 = 1.32 > Fr_c$, see Table 1 and Fig. 9(c)) due to the characteristics of this area over Rockies (Fig. 8). The layer structure for Case C is more complex than other cases in that there are multiple vertical shear layers: i.e. positive shear near the surface and between 9 km and 19 km, and negative shear elsewhere (Fig. 10(b)). The overall structure of the static stability is similar to other cases (Fig. 10(a)).

The simulated and parametrized momentum flux profiles (for $Ri_c = 1$) show a relatively close match. Ri_m is very large at upper levels (Fig. 11), which means wave-breaking is absent at upper levels as confirmed in the simulation (Fig. 9(c)). The magnitude of the surface flux is much smaller than Case A and similar to (and smaller than) Case B, due to weaker LLWB associated with orographic anisotropy. The parametrization realistically estimates the magnitude of the reference-level drag and its vertical divergence; however, below the reference level BLD is somewhat underestimated as in Case B. We note here that it is fairly easy to retune BLD by a factor of two for Cases B and C. The easiest way is perhaps to eliminate the factor $1/2$ from Eq. (12) or increase the value of C_d to 2.0 to double the magnitude. This will, however, overestimate the BLD for Case A by a factor of two. We always try to prevent overestimation and allow for underestimation. On the other hand, our GWD formulation shows less of this dilemma of overestimation versus underestimation, as seen in Fig. 12 (and later in Fig. 13).

The results of Cases B and C imply that BLD parametrized by our formulation is relatively less dependent on orographic anisotropy and is somewhat harder to parametrize, while low-level GWD is more dependent on orographic anisotropy and is relatively easier to parametrize. This is consistent with our experience that an implementation of large isotropic BLD into NOGAPS tends to improve the forecast skill.

(iv) *Evaluation of all time episodes including Cases A, B and C*. In addition to the detailed evaluation of the above case-studies, the magnitudes of the reference-level drag parametrized by the KA95+ scheme (Eq. (6)) is also evaluated by simple linear regression for all times taken from the explicit simulations. These cases include not only wave-breaking and trapping cases, but also fairly linear cases with very weak or virtually

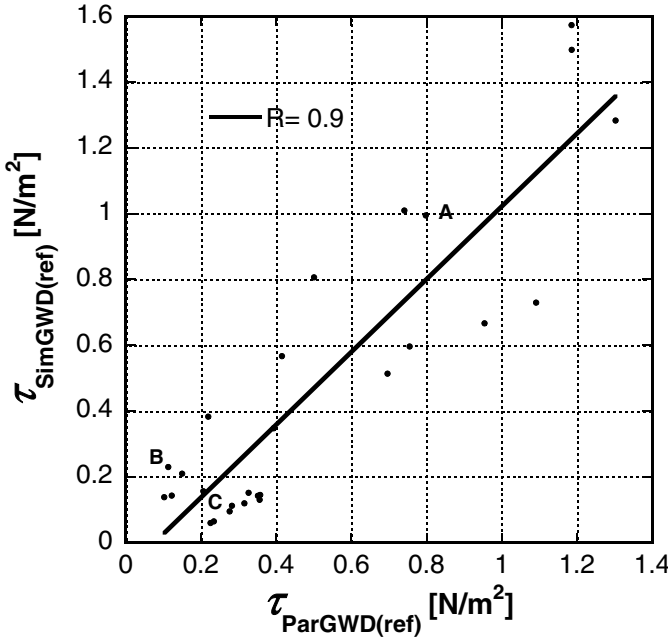


Figure 13. The parametrized gravity-wave drag (GWD) at the reference level (abscissa) versus the explicitly simulated domain-averaged GWD at the reference level (ordinate). A total of twenty-six snapshots have been taken at various times with 3- or 6-hour interval from the mesoscale simulations performed with COAMPS®, including Cases A (06 UTC 28 December 1998), B (00 UTC 31 October 1998) and C (12 UTC 01 January 1999) as marked in the diagram. R is the linear correlation coefficient of the least-square curve fit.

no wave activity (not shown). As shown in Fig. 13, which consists of 26 ‘snapshots’ taken from the simulations, the correlation between the parametrization and simulation, including Cases A, B and C, is very high (with correlation coefficient ≈ 0.9).

(d) Flow regime diagram

There are different sources of drag due to subgrid-scale orography currently considered together with GWD parametrization: BLD due to low-level flow blocking, GWD due to breaking at upper levels of vertically propagating hydrostatic waves, GWD due to LLWB, GWD due to non-hydrostatically trapped waves or drag due to internal reflection, critical-level absorption, and orographic lift, etc. Figure 1 shows some of these sources schematically (see also Fig. 4 of Kim *et al.* (2003) and Fig. 1 of Zadra *et al.* (2003)). The parametrizations by MW96 and GSM98, which follow Shutts (1990), include several sources of drag (GWD due to hydrostatic waves, LLWB, trapped lee waves, and internal wave reflection), while SM00 includes BLD, non-hydrostatic and hydrostatic GWD; LM97 includes BLD and hydrostatic GWD. The KA95+ parametrization includes all of these, but GWD due to hydrostatic and non-hydrostatic waves is treated collectively. The relationship or harmony among these mechanisms, at low levels in particular, can be understood using a ‘regime diagram’ as shown, for example, in Fig. 1 of SM00 and Fig. 2 of LM97. In a regime diagram, the surface pressure drag is non-dimensionalized by its linear counterpart, and plotted as a function of the inverse Froude number in order to identify the flow regimes, e.g. MJ92; Stein 1992, hereafter S92; OB96/97; LM97; SM00). This diagram serves as an effective measure to check the overall behaviour of drag parametrization schemes for a variety of

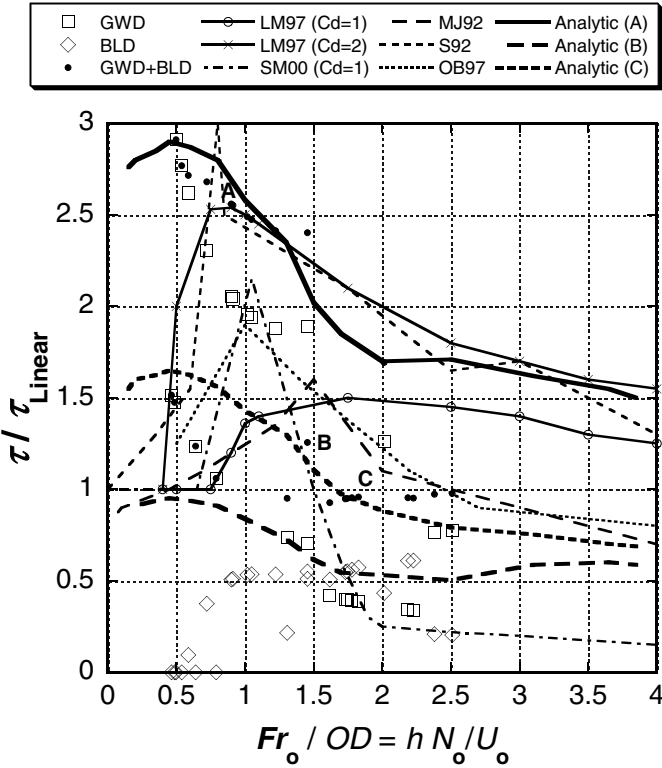


Figure 14. Flow regime diagram that shows the ratio of parametrized GWD at the reference level and/or BLD to the linear drag as a function of the domain-averaged low-level inverse Froude number, defined by Eq. (5), but divided by OD . Total of twenty-six ‘snapshots’ have been taken at various times with 3- or 6-hour intervals from the mesoscale simulations performed with COAMPS®, including Cases A (06 UTC 28 December 1998), B (00 UTC 31 October 1998) and C (12 UTC 01 January 1999) as marked in the diagram. The curves for MJ92, S92 and LM97 have been reconstructed from Fig. 2 of LM97 while those for OB97 and SM00 have been reconstructed from Fig. 7(a) of SM00. The thick solid, long-dashed and short-dashed curves (corresponding respectively to Cases A, B and C) are obtained from the analytic version of the parametrization (GWD+BLD) by analytically varying wind and stability, but with basic orographic statistics fixed (Table 1). See text for further details.

flow states. SM00 categorized the flow over orography depending on the low-level value of the Froude number: when Fr_0 is smaller than its critical value (typically, $Fr_c \approx 0.8$) the regime is governed by linear dynamics; when Fr_0 is between Fr_c and a typical threshold value (of less than 2) the regime is governed by nonlinear dynamics and the drag becomes at least twice the linear value; when Fr_c is greater than the threshold value the regime is considered to be governed by near-surface-flow dynamics, while it is recognized that there can be significant overlap between the last two regimes.

Figure 14 shows such a diagram obtained from the KA95+ scheme using all times of the explicit simulations, including Cases A, B and C, in comparison with results from selected other studies. Note that Fr_0 defined by Eq. (5) has been divided by OD (Eq. (4)) to make it comparable to other studies. For the linear drag, we use the expression for the 2-D hydrostatic non-rotating frictionless GWD, $\kappa \rho_0 N_0 U_0 \sigma_h^2$ with $\kappa = 8 \times 10^{-6}$ (McFarlane 1987). Note that the magnitudes of our non-dimensional drag depend on our choice of κ , and thus the comparison made with other studies can only be relative. Our results show that the total drag is clearly divided into two groups; the upper one with values greater than 2.0, and the lower one smaller than 2.0. These groups correspond

directly to values of OD which are greater and smaller, respectively, than its average value of 1.08 with four directions. Some key features of the upper group are also found in other studies, such as the drastic increase of the reference-level drag near the critical value of Fr_0 ($= 0.8$) and gradual decrease of the drag as Fr_0 increases further (e.g. LM97 for $C_d = 2$ and S92 on the diagram). In these results that involve smaller values of Fr_0 , GWD is several times greater than BLD as is also shown by SM00 (see their Fig. 7(a)); whereas in the lower group results with smaller non-dimensional drag and larger values of Fr_0 , GWD is roughly comparable to BLD. This shows that GWD is dominant for smaller Fr_0 , but BLD becomes equally dominant for larger Fr_0 . Webster *et al.* (2003) introduced a simple parametrization in which the magnitude of BLD is inversely proportional to that of GWD, which is consistent with our results except that their BLD is larger than GWD. We also constructed the diagram with respect to the original definition of Fr_0 by Eq. (5) and found qualitatively similar results, except that the lower group is displaced to left on the diagram by about 0.5 of a Froude number unit (not shown). Moreover, we found virtually no correlation between Fr_0 and OD . This suggests that the magnitude of the drag depends largely on orographic anisotropy, regardless of Fr_0 . Since OD enters into our scheme only through Fr_0 , the magnitude of drag is well controlled by OD in the scheme, as shown in the comparison with the explicit simulations (see Fig. 13). Our results also imply that there can be large differences between 3-D and 2-D orography in the magnitudes of drag as shown by earlier studies, and also illustrated by the two distinct groups of points in Fig. 14. For example, MJ92, OB97, LM97 ($C_d = 1$) and SM00 (large Fr_0 portion) correspond to our 3-D results whereas S92, LM97 ($C_d = 2$) and SM00 (small Fr_0 portion) correspond to our 2-D results.

Furthermore, for a more instructive comparison with other studies, we fixed basic orographic statistics and analytically varied the wind and stability for the three Cases (A, B and C, see Table 1), although a regime diagram constructed this way with our scheme may not be very realistic since some orographic statistics cannot be analytically obtained. The analytic drag curves (denoted by thick curves in Fig. 14) are, overall, comparable to our actual simulation results except for Case B (thick long-dashed curve), which is only about the half of the simulated value (marked by B on the diagram). This is probably due to the fact that, although the orientation of the main mountain ridges gives a rather small value of OD (i.e. the horizontal mountain aspect ratio), the complex nature of the orography in the domain contributes to fairly nonlinear and vertically propagating behaviour of the waves as can be seen in Fig. 9(b), which is not well represented by the crude analytic formula. In addition, the analytic drag curve for Case A (thick solid curve) roughly follows the upper drag group of other studies (somewhat smaller between $1.2 < Fr_0 < 2.5$) except for Fr_0 smaller than ~ 0.8 , which is significantly larger than other studies. On the other hand, the curve for Case C (thick short-dashed curve) runs through the lower group while that for Case B (thick long-dashed curve) generally goes below the lower group. It is evident that our peak value of the analytic drag is located at a smaller value of Fr_0/OD than other studies. This may be due partially to the effect of OD , and also to the mathematical nature of our formulation that gives large values for small values of the static stability (see Eq. (6)).

(e) Weighted averages of the orographic statistics

In the introduction, we discussed that column (i.e. local) GWD parametrizations become increasingly hard to justify as model resolution increases and we introduce a non-local version of the scheme in appendix A. For computational reasons under the parallel computing architecture, however, our GWD parametrization currently remains

local. The sensitivity of OA and L_x to the location of orography relative to the grid is in practice effective for distinguishing different typical near-surface flow states, but it is undesirable in principle: it would be better if the total drag were to be independent of the relative location of orography and grid. A very crude way to alleviate this deficiency is to apply global smoothing to the global drag field at the end of each time step, which may in some sense be similar to using the non-local version of the scheme presented in appendix A. A more refined method, however, is to take a weighted average of the orographic statistics also including orography of nearby grid boxes depending on the wind direction. Moreover, the choice of eight predetermined directions to calculate OA and L_x was mainly motivated by its simplicity, and also our experience that too detailed wind directions can excessively constrain the subgrid-scale wind directions that change locally. This choice, however, may invoke a sudden jump in the value of the orographic statistics with a small change in the wind direction. A weighted average of the statistics will reduce this effect. Appendix B introduces an example of such weighting procedure.

The weighting tends to smooth the orographic statistics and slightly increase or decrease the aspect ratio depending on the region. We compared the new parametrization results using the ‘weighted’ statistics of OA , L_x (and h_c) with the original formulations (see Fig. 12). Overall, the GWD parametrization is similar to the original one, while the BLD parametrization produces larger differences than the GWD counterpart. The BLD parametrization is more sensitive to the weighting (through L_x^\perp) than the GWD parametrization, and thus may require further calibration for improvement.

(f) *Effects of moisture*

Durran and Klemp (1982a) investigated the effects of moisture in the development of trapped mountain waves, and reported that the wave response can be amplified or damped depending on the environment and the height. We investigate this effect by performing an additional simulation of Case A with moisture included (Fig. 15(a)) and comparing it with the dry counterpart (Fig. 12(a)). We find some noticeable differences due to moisture in the development of waves such as: larger wave amplitudes, more lateral spreading and breaking of wave packets especially at upper levels, and some differences shown in the domain-averaged momentum flux profile mostly in the middle levels (Fig. 15(b)). The parametrization appears to be less responsive to vertical drag divergence between 15 and 7 km when moisture is present.

Durran and Klemp (1982b) derived a modified Brunt–Väisälä frequency that includes the moisture contribution to account for the effect of moisture. Surgi (1989) also formulated a moist Brunt–Väisälä frequency (N_m) for use in an orographic GWD parametrization scheme as an effective way of vertically redistributing GWD due to moisture. We implemented this formulation in which the dry Brunt–Väisälä frequency (N_d) is multiplied by a factor as follows:

$$N_m = (1 - \varepsilon)^{1/2} N_d, \quad (14)$$

where ε is 0.1, 0.2 or 0.3 for a high-, middle- or low-cloud layer, respectively (Surgi 1989). We found the use of Eq. (14) in the scheme slightly reduces/increases the magnitude of the drag at lower/upper levels, which corrects the slightly overestimated flux at low levels (Fig. 15(b)). Our test result, while limited, suggests that the pragmatic assumption made in virtually all of the GWD parametrization schemes that ignore the effects of moisture may be valid only to a first order of approximation. Consequently the parametrizations may need to be re-evaluated to fully incorporate the effect of moisture.

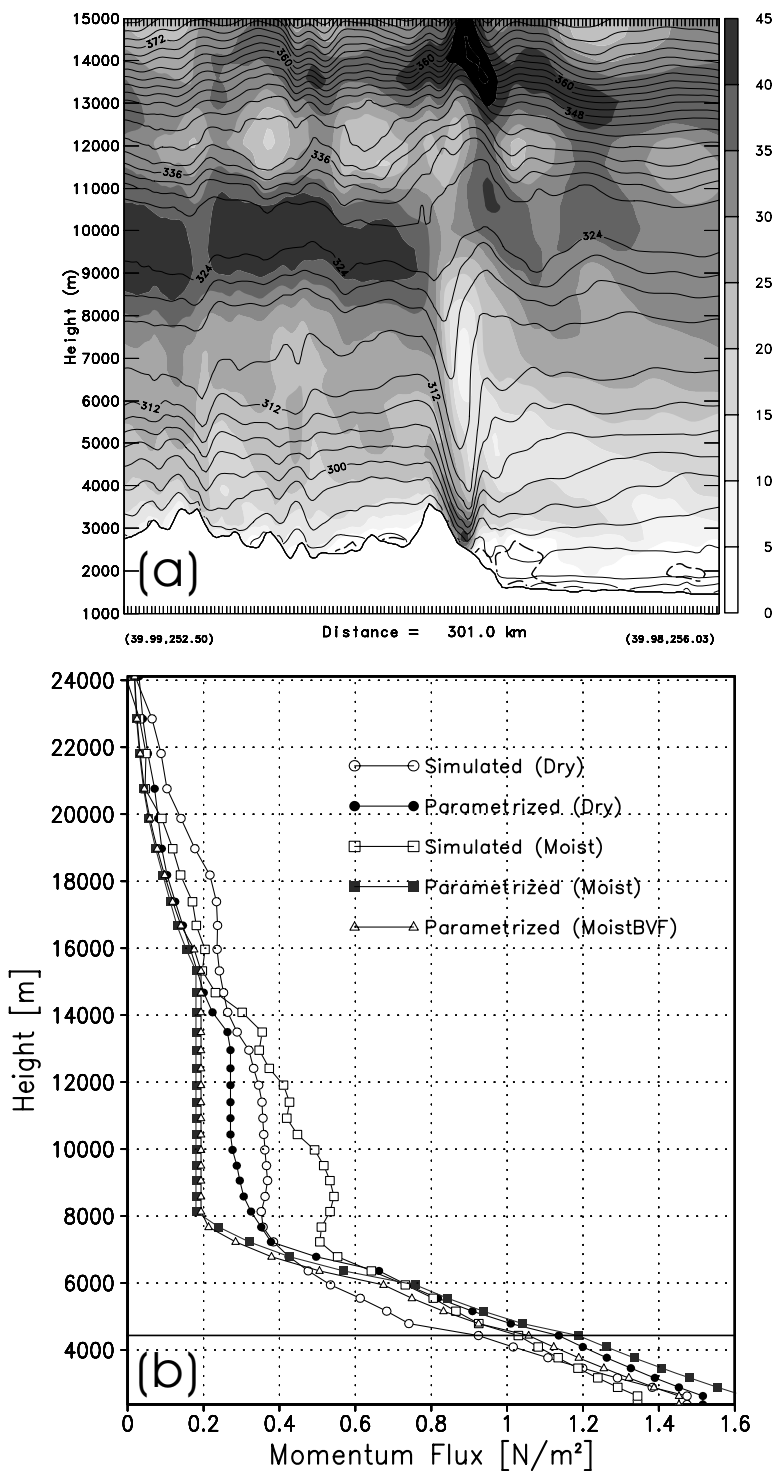


Figure 15. (a) As in Fig. 9(a) for Case A (06 UTC 28 December 1998), but with moisture included; (b) as in Fig. 12(a) (dry), but also with moisture included, together with the moist Brunt–Väisälä frequency adjusted as given by Eq. (14).

5. CONCLUDING REMARKS

Evaluation of an orographic drag parametrization scheme in a large-scale model is challenging, since its success often depends on its harmony with other model physics as well as its own physical adequacy. Evaluations with mesoscale models and observations of proven quality are, therefore, a logical course of research. Perhaps, a community-wide joint intercomparison effort with well-established mesoscale models will be useful to further advance the parametrization.

The KA95 and KA95+ orographic-drag parametrization scheme is basically a statistical fit of physically constrained, semi-empirical formulations to mountain-wave simulations. The results presented in this study are highly encouraging. There remain, however, issues in the design and evaluation of the extended scheme. As described in subsections 2(a), 4(e) and appendix A, further study is required to fully include the non-local effect of drag under the parallel computing architecture. Further, as discussed in subsection 4(e), the sensitivity of the orographic statistics to the relative location of orography is not desirable in principle, and an approximate method to alleviate this deficiency has been presented in appendix B. The scheme also needs to be evaluated offline for other regions with more diverse values of orographic anisotropy than the four values used in this study.

In this study we did not investigate the simulated momentum flux profile below the mountain crest. Rather, we compared explicitly calculated surface pressure drag with parametrized BLD below the crest as an effort to evaluate the parametrization. However, Laprise and Peltier (1989) discussed as an extension of the Eliassen–Palm theorem that, below the crest of a mountain, the sum of the vertical profiles of Reynolds stress—which is calculated excluding underground points—and (wave) pressure drag is approximately constant in height for stationary state conditions in the absence of lateral boundary fluxes (see their Fig. 19). It may be worthwhile to systematically verify this argument against explicit simulations.

It has been justified that BLD is a more physical representation of the orographic blocking effect in the subgrid-scale (e.g. LM97), compared with an earlier method of enhancing resolved-scale orography, such as envelope or silhouette orography. Orographic roughness parametrizations are widely used to represent enhanced surface friction (e.g. MW96; GSM98) although they may suffer from deficiencies in some other applications due to its temporally invariant nature as pointed out by Boer and Lazare (1988). Despite the inherent differences discussed in the introduction, orographic roughness parametrizations are sometimes expected to perform a function similar to BLD (as noted from the fact that it is often called form drag). It is also found that some BLD schemes are being used together with form-drag formulations. The interaction among all of the drag mechanisms parametrized near the surface, such as friction drag, form drag, BLD, GWD, drag associated with convectively generated gravity waves (e.g. Chun *et al.* 2004) and even convective momentum transport (Gregory *et al.* 1997), etc. is complex and not yet clearly understood; accordingly they are not fully represented in large-scale models. As implied by the discussion in the literature related to the interpretation of the regime diagram as well as the relationship between BLD and form drag (e.g. LM97, GSM98, SM00, Webster *et al.* 2003), more work is needed on including the effects of gravity-wave processes in large-scale models.

The original KA95 scheme is currently part of the NCEP (National Centers for Environmental Prediction) global forecast models (Alpert *et al.* 1996; Kanamitsu *et al.* 2002). The extended scheme (KA95+) presented in this study is being tested with the ALPHA version of NOGAPS (Eckermann *et al.* 2004), which now uses the mean orography (Kim and Hogan 2004).

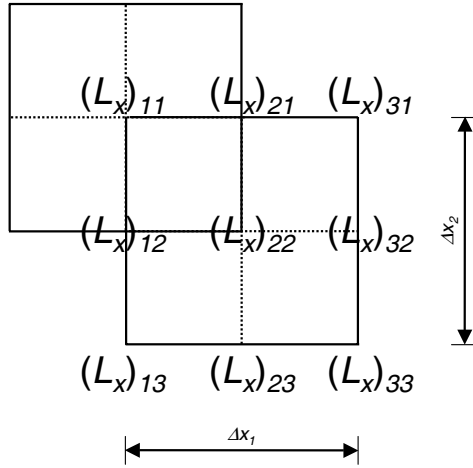


Figure A.1. A staggered grid for weighting of the effective orographic length L_x (Fig. 7). Shown are a grid box (domain) centred at point 22 and an example of a box centred at point 11, which is shifted from 22 by half grid interval in both directions. See text for further details.

APPENDIX A

Inclusion of the non-local effect in the KA95/KA95+ GWD parametrization scheme

Due to the non-local nature of gravity waves that can propagate out of or into a grid box column, the inclusion of the influence of the waves on neighbouring grid columns may be an important issue in GWD parametrizations (see subsection 2(a)). For example, if the model grid were placed as shown by the dashed line in Fig. A.1 the GWD generated by the mountain in the left-side grid domain would reach the right-side grid domain where no mountain is present. Kim (1992) incorporated this effect by regarding the orographic asymmetry, OA , as a free parameter and obtaining the expected value of the parametrized drag (τ_{GWD}) for the entire range of OA . The integration of τ_{GWD} over OA includes the contribution of OA due to orography not only in the corresponding grid cell, but also in the neighbouring grid cell along the direction of the low-level wind. Mathematically, it can be expressed as:

$$E(\tau_{\text{GWD}}) = \frac{1}{OA_{\text{max}} - OA_{\text{min}}} \int_{OA_{\text{min}}}^{OA_{\text{max}}} \tau_{\text{GWD}}(OA) d(OA), \quad (\text{A.1})$$

where OA (Eq. (1)) is normalized, i.e. $OA_{\text{max}} = 1$ and $OA_{\text{min}} = -1$.

The expected value of τ_{GWD} (Eq. (6)) is obtained numerically using Eq. (A.1) for a discrete set of OAs between OA_{max} and OA_{min} (e.g. varying from -1 to $+1$ with an interval of 0.1) and also using the averages of the flow parameters (i.e. N , U , and Fr_0) extending over to the upstream and/or downstream grid cell, possibly depending on the location of the bulk orography (i.e. the sign of the local value of OA). In the example shown in Fig. A.1, where the orography is near the downstream cell boundary ($OA \approx -1$), the averages of the flow parameters are taken over the larger grid cell extended downstream. A series of comparisons were made between the original (Eq. (6)) and non-local (Eq. (A.1)) versions off-line, and also on-line with a non-parallelized version of a general circulation model (Kim 1992). It was found that two versions produce quantitatively different but qualitatively similar results, particularly in respect of the impact on the large-scale simulations. Implementation of this expression into

a massively parallelized model code, however, causes significant degradation of the computational efficiency due to the required communication with neighbouring grid cells at each time step. Improved optimization methods are needed to overcome this technical difficulty.

APPENDIX B

Weighted averages of the orographic statistics

In order to make the effective orographic length (L_x) less local (see subsection 4(e)), we consider a staggered grid shown in Fig. A.1. L_x can be calculated with weighting for the representative wind directions (Fig. 6) as:

$$\begin{aligned} W : & \omega_1(L_x)_{23} + \omega_2(L_x)_{22} + \omega_1(L_x)_{21} \\ S : & \omega_1(L_x)_{12} + \omega_2(L_x)_{22} + \omega_1(L_x)_{32} \\ SW : & \omega_1(L_x)_{11} + \omega_2(L_x)_{22} + \omega_1(L_x)_{33} \\ NW : & \omega_1(L_x)_{13} + \omega_2(L_x)_{22} + \omega_1(L_x)_{31}, \end{aligned} \tag{B.1}$$

where ω_1 and ω_2 are the weighting coefficients ($2\omega_1 + \omega_2 = 1$) for which we choose 0.25 and 0.5, respectively. Furthermore h_c , which is calculated similarly to L_x with respect to predetermined wind directions (Fig. 6), can also be weighted following Eq. (B.1).

For taking a weighted average of OA , we use either Eq. (B.1) or the following expression based on Fig. 2:

$$\begin{aligned} W : & \omega_1 OA_{NW} + \omega_2 OA_W + \omega_1 OA_{SW} \\ S : & \omega_1 OA_{SW} + \omega_2 OA_S + \omega_1 OA_{SE} \\ SW : & \omega_1 OA_W + \omega_2 OA_{SW} + \omega_1 OA_S \\ NW : & \omega_1 OA_N + \omega_2 OA_{NW} + \omega_1 OA_W, \end{aligned} \tag{B.2}$$

where ω_1 and ω_2 are 0.125 and 0.75, respectively. Note that the weighting coefficients for OA are different from those of L_x , due to the difference between OA and L_x in the subgrid boxes considered for counting the orographic height points. We also tested the method used above for L_x to calculate OA and found qualitatively similar results. Use of these formulations will make the orographic statistics more robust.

ACKNOWLEDGEMENTS

The first and second authors acknowledge the supports from the sponsor, the Office of Naval Research under ONR Program Elements 0602435N and 0601153N, respectively. The first author wishes to express much delayed gratitude to Drs J. Alpert and S.-Y. Hong for their aid in implementing his original scheme into NCEP global models. He also appreciates discussions with Drs T. Hogan, J. Scinocca and S. Webster. The authors thank the two anonymous reviewers and Dr N. Wood who provided comments that led to significant improvement of the manuscript, particularly regarding the robustness of the orographic statistics. The computing time was supported in part by a grant of HPC time from the DoD MSRC at Aberdeen, MD, USA.

REFERENCES

- Alpert, J. C. 2004 'Sub-grid scale mountain blocking at NCEP'. (CD-ROM) Proceedings of the 16th conference on NWP, 11–15 January 2004, Seattle, Washington. American Meteorological Society, Boston, USA
- Alpert, J. C., Hong, S.-Y. and Kim, Y.-J. 1996 'Sensitivity of cyclogenesis to lower tropospheric enhancement of gravity wave drag using the environmental modeling center medium range model'. Pp. 322–323 in Preprints of the 11th conference on NWP, 19–23 August 1996, Norfolk, Virginia. American Meteorological Society, Boston, USA
- Baines, P. G. and Palmer, T. N. 1990 'Rationale for a new physically based parameterization of sub-grid scale orographic effects'. Technical memorandum 169. European Centre for Medium-Range Weather Forecasts, Shinfield, Reading, UK
- Belcher, S. E. and Hunt, J. C. R. 1998 Turbulent flow over hills and waves. *Ann. Rev. Fluid Mech.*, **30**, 507–538
- Boer, G. J. and Lazare, M. 1988 Some results concerning the effect of horizontal resolution and gravity-wave drag on simulated climate. *J. Climate*, **1**, 789–806
- Boer, G. J., McFarlane, N. A., Laprise, R., Henderson, J. D. and Blanchet, J.-P. 1984 The Canadian Climate Centre spectral atmospheric general circulation model. *Atmos.-Ocean*, **22**, 397–429
- Bretherton, F. P. 1969 Momentum transport by gravity waves. *Q. J. R. Meteorol. Soc.*, **95**, 213–243
- Broad, A. S. 1996 High-resolution numerical-model integrations to validate gravity-wave-drag parameterization schemes: A case study. *Q. J. R. Meteorol. Soc.*, **122**, 1625–1653
- Brown, A. R. and Webster, S. 2004 Orographic flow-blocking scheme characteristics. *Q. J. R. Meteorol. Soc.*, **130**, 3015–3028
- Chun, H.-Y., Song, I.-S., Baik, J.-J. and Kim, Y.-J. 2004 Impact of a convectively forced gravity-wave drag parameterization in NCAR CCM3. *J. Climate*, **17**, 3529–3546
- Davies, H. C. 1976 A lateral boundary formulation for multi-level prediction models. *Q. J. R. Meteorol. Soc.*, **102**, 405–418
- Doyle, J. D. and Durran, D. R. 2002 The dynamics of mountain wave-induced rotors. *J. Atmos. Sci.*, **59**, 186–201
- Doyle, J. D., Durran, D. R., Chen, C., Colle, B. A., Georgelin, M., Grubisic, V., Hsu, W. R., Huang, C. Y., Landau, D., Lin, Y. L., Poulos, G. S., Sun, W. Y., Weber, D. B., Wurtele, M. G. and Xue, M. 2000 An intercomparison of model-predicted wave breaking for the 11 January 1972 Boulder windstorm. *Mon. Weather Rev.*, **128**, 901–914
- Doyle, J. D., Volkert, H., Dörnbrack, A., Hoinka, K. P. and Hogan, T. F. 2002 Aircraft measurements and numerical simulations of mountain waves over the central Alps: A pre-MAP test case. *Q. J. R. Meteorol. Soc.*, **128**, 2175–2184
- Durran, D. R. and Klemp, J. B. 1982a The effects of moisture on trapped mountain lee waves. *J. Atmos. Sci.*, **39**, 2490–2506
- 1982b On the effects of moisture on the Brunt–Väisälä frequency. *J. Atmos. Sci.*, **39**, 2152–2158
- Eckermann, S. D., McCormack, J. P., Coy, L., Allen, D., Hogan, T. F. and Kim, Y.-J. 2004 'A prototype high-altitude global NWP model'. In Proceedings of the symposium on the 50th anniversary of operational numerical weather prediction 14–17 June, 2004. American Meteorological Society, University of Maryland, College Park, MD, USA
- Gregory, D., Kershaw, R. and Inness, P. M. 1997 Parameterization of momentum transport by convection. II: Tests in single-column and general circulation models. *Q. J. R. Meteorol. Soc.*, **123**, 1153–1183
- Gregory, D., Shutts, G. J. and Mitchell, J. R. 1998 A new gravity-wave-drag scheme incorporating anisotropic orography and low-level wave breaking: impact upon the climate of the UK Meteorological Office Unified Model. *Q. J. R. Meteorol. Soc.*, **124**, 463–493
- Hodur, R. M. 1997 The Naval Research Laboratory's Coupled Ocean/Atmosphere Mesoscale Prediction System (COAMPS). *Mon. Weather Rev.*, **125**, 1414–1430

- Hogan, T. F. and Rosmond, T. 1991 The description of the Navy Operational Global Atmospheric Prediction System's spectral forecast model. *Mon. Weather Rev.*, **119**, 1186–1815
- Hunt, J. C. R. and Snyder, W. H. 1980 Experiments on stably stratified flow over a model three-dimensional hill. *J. Fluid Mech.*, **96**, 671–704
- Iwasaki, T. and Sumi, A. 1986 Impact of envelope orography on JMA's hemispheric NWP forecasts for winter circulation. *J. Meteorol. Soc. Jpn.*, **64**, 245–258
- Kanamitsu, M., Kumar, A., Juang, H.-M. H., Schemm, J.-K., Wang, W., Yang, F., Hong, S.-Y., Peng, P., Chen, W., Moorthi, S. and Ji, M. 2002 NCEP dynamical seasonal forecast system 2000. *Bull. Am. Meteorol. Soc.*, **83**, 1019–1037
- Kim, Y.-J. 1992 Numerical simulation and parameterization of orographic gravity waves. PhD dissertation, University of California, Los Angeles
- 1996 Representation of subgrid-scale orographic effects in a general circulation model: Part I. Impact on the dynamics of simulated January climate. *J. Climate*, **9**, 2698–2717
- Kim, Y.-J. and Arakawa, A. 1994 'Inclusion of the effect of low-level wave-breaking in orographic gravity wave parameterization for large-scale models of the atmosphere'. Pp. 386–388 in Preprints of the tenth conference on NWP, July 18–22, Portland, Oregon. American Meteorological Society, Boston, USA
- 1995 Improvement of orographic gravity-wave parameterization using a mesoscale gravity-wave model. *J. Atmos. Sci.*, **52**, 1875–1902
- Kim, Y.-J. and Hogan, T. F. 2004 Response of a global atmospheric forecast model to various drag parameterizations. *Tellus*, **56A**, 472–484
- Kim, Y.-J., Eckermann, S. D. and Chun, H.-Y. 2003 An overview of the past, present and future of gravity-wave drag parameterization for numerical climate and weather prediction models. *Atmos-Ocean*, **41**, 65–98
- Lane, T. P., Reeder, M. J., Morton, B. R. and Clark, T. L. 2000 Observations and numerical modeling of mountain waves over the Southern Alps of New Zealand. *Q. J. R. Meteorol. Soc.*, **126**, 2765–2788
- Laprise, R. and Peltier, W. R. 1989 The structure and energetics of transient eddies in a numerical simulation of breaking mountain waves. *J. Atmos. Sci.*, **46**, 565–585
- Leutbecher, M. and Volkert, H. 2000 The propagation of mountain waves into the stratosphere: Quantitative evaluation of three-dimensional simulations. *J. Atmos. Sci.*, **57**, 3090–3108
- Lilly, D. K. and Zipser, E. J. 1972 The Front Range windstorm of 11 January 1972—a meteorological narrative. *Weatherwise*, **25**, 56–63
- Lindzen, R. S. 1981 Turbulence and stress owing to gravity wave and tidal breakdown. *J. Geophys. Res.*, **86**, 9707–9714
- Lott, F. and Miller, M. J. 1997 A new subgrid-scale orographic parameterization: Its formulation and testing. *Q. J. R. Meteorol. Soc.*, **123**, 101–127
- McFarlane, N. A. 1987 The effect of orographically excited gravity-wave drag on the general circulation of the lower stratosphere and troposphere. *J. Atmos. Sci.*, **44**, 1775–1800
- Milton, S. F. and Wilson, C. A. 1996 The impact of parameterized subgrid-scale orographic forcing on systematic errors in a global NWP model. *Mon. Weather Rev.*, **124**, 2023–2045
- Miranda, P. M. A. and James, I. N. 1992 Nonlinear three-dimensional effects on gravity waves: Splitting flow and breaking waves. *Q. J. R. Meteorol. Soc.*, **118**, 1057–1081
- Nance, L. B. and Durran, D. R. 1998 A modeling study of nonstationary trapped mountain lee waves. Part II: Nonlinearity. *J. Atmos. Sci.*, **55**, 1429–1445
- Nappo, C. J. and Chimonas, G. 1992 Wave exchange between the ground surface and a boundary-layer critical level. *J. Atmos. Sci.*, **49**, 1075–1091
- Ólafsson, H. and Bougeault, P. 1996 Nonlinear flow past an elliptic mountain ridge. *J. Atmos. Sci.*, **53**, 2465–2489
- 1997 The effect of rotation and surface friction on orographic drag. *J. Atmos. Sci.*, **54**, 193–210

- Palmer, T. N. and Mansfield, D. A. 1986 A study of wintertime circulations anomalies during past El Niño events, using a high resolution general circulation model. I: Influence of model climatology. *Q. J. R. Meteorol. Soc.*, **112**, 613–638
- Palmer, T. N., Shutts, G. J. and Swinbank, R. 1986 Alleviation of a systematic westerly bias in general circulation and numerical weather prediction models through an orographic gravity-wave drag parameterization. *Q. J. R. Meteorol. Soc.*, **112**, 1001–1039
- Peltier, W. R. and Clark, T. L. 1979 The evolution and stability of finite-amplitude mountain waves. Part II: Surface-wave drag and severe downslope windstorms. *J. Atmos. Sci.*, **36**, 1498–1529
- Peng, M. S. and Thompson, W. T. 2003 Some aspects of the effect of surface friction on flows over mountains. *Q. J. R. Meteorol. Soc.*, **129**, 2527–2557
- Phillips, D. S. 1984 Analytical surface pressure and drag for linear hydrostatic flow over three-dimensional elliptical winters. *J. Atmos. Sci.*, **41**, 1073–1084
- Pierrehumbert, R. T. 1986 'An essay on the parameterization of orographic gravity-wave drag'. Pp. 251–282 in volume 1 of the Proceedings of the seminar/workshop on observation, theory and modelling of orographic effects. ECMWF, Shinfield Park, Reading, UK
- Richard, E., Mascart, P. and Mickerson, E. C. 1989 The role of surface friction in downslope windstorms. *J. Appl. Meteorol.*, **28**, 241–251
- Schär, C. and Durran, D. R. 1997 Vortex formation and vortex shedding in continuously stratified flows past isolated topography. *J. Atmos. Sci.*, **54**, 534–554
- Schär, C. and Smith, R. B. 1993 Shallow water flow past isolated topography. Part I: Vorticity production and wave formation. *J. Atmos. Sci.*, **50**, 1373–1400
- Scinocca, J. F. and McFarlane, N. A. 2000 The parameterization of drag induced by stratified flow over anisotropic topography. *Q. J. R. Meteorol. Soc.*, **126**, 2353–2393
- Scorer, R. S. 1949 Theory of lee waves of mountains. *Q. J. R. Meteorol. Soc.*, **75**, 41–56
- Shutts, G. J. 1990 'A new gravity-wave drag parameterization scheme for the Unified Model'. Turbulence and diffusion note 2, Available from APR-Div., Meteorological Office, Exeter, UK
- 1998 Stationary gravity-wave structure in flows with directional wind shear. *Q. J. R. Meteorol. Soc.*, **124**, 1421–1442
- Shutts, G. J. and Broad, A. S. 1993 A case study of lee waves over the Lake District in northern England. *Q. J. R. Meteorol. Soc.*, **119**, 377–408
- Smolarkiewicz, P. K. and Rotunno, R. 1989 Low Froude number flow past three dimensional obstacles. Part I: Baroclinically generated lee vortices. *J. Atmos. Sci.*, **46**, 1154–1164
- Stein, J. 1992 Investigation of the regime diagram of hydrostatic flow over a mountain with a primitive equation model. Part I: Two-dimensional flows. *Mon. Weather Rev.*, **120**, 2962–2976
- Surgi, N. 1989 Systematic errors of the FSU global spectral model. *Mon. Weather Rev.*, **117**, 1751–1766
- Tibaldi, S. 1986 Envelope orography and the maintenance of quasi-stationary waves in the ECMWF model. *Adv. Geophys.*, **29**, 339–374
- Wallace, J., Tibaldi, S. and Simmons, A. 1983 Reduction of systematic forecast errors in the ECMWF model through the introduction of an envelope orography. *Q. J. R. Meteorol. Soc.*, **109**, 683–717
- Webster, S., Brown, A. R., Cameron, D. R. and Jones, C. P. 2003 Improvements to the representation of orography in the Met Office Unified Model. *Q. J. R. Meteorol. Soc.*, **129**, 1989–2010
- Wood, N. and Mason, P. J. 1993 The pressure force induced by neutral turbulent flow over hills. *Q. J. R. Meteorol. Soc.*, **119**, 1233–1267
- Zadra, A., Roch, M., Laroche, S. and Charron, M. 2003 The subgrid-scale orographic blocking parameterization of the GEM model. *Atmos.-Ocean*, **41**, 155–170